CrossMark

**ORIGINAL ARTICLE**

**Nima Tofighi · Murat Ozbulut ·
James J. Feng · Mehmet Yildiz**

# The effect of normal electric field on the evolution of immiscible Rayleigh-Taylor instability

**Abstract** Manipulation of the Rayleigh-Taylor instability using an external electric field has been the subject of many studies. However, most of these studies are focused on early stages of the evolution. In this work, the long-term evolution of the instability is investigated, focusing on the forces acting on the interface between the two fluids. To this end, numerical simulations are carried out at various electric permittivity and conductivity ratios as well as electric field intensities using Smoothed Particle Hydrodynamics method. The electric field is applied in parallel to gravity to maintain unstable evolution. The results show that increasing top-to-bottom permittivity ratio increases the rising velocity of the bubble while hindering the spike descent. The opposite trend is observed for increasing top-to-bottom conductivity ratio. These effects are amplified at larger electric field intensities, resulting in narrower structures as the response to the excitation is non-uniform along the interface.

## 1 Introduction

An interface between two immiscible fluids may be subject to capillary, viscous and gravitational forces, depending on the flow configuration. Manipulation of this interface by introducing an external electric field has been of great interest. Earlier works on this subject have been carried out by Taylor [1], who proposed the leaky dielectric model. Melcher conducted further studies on the effects of tangential and perpendicular fields on the interface [2,3]. A review of several flow configurations are provided by Saville [4]. Some examples of the applications of electrically manipulated interfaces are found in spraying [5,6], flow focusing [7], dispersion [8], micromixing [9–11] and pattern formation [12,13], to name a few.

The manipulation of the interface with the electric field is highly dependent upon the orientation of the electric field with respect to the interface and the electrical properties of the fluids in question. The electric field may be parallel or perpendicular to the initially undisturbed interface, while the fluids may be either perfect or leaky dielectrics. Pease and Russel [14] investigated the pattern formation in leaky and perfect dielectric

---

Communicated by Oleg Zikanov.

N. Tofighi · M. Ozbulut · M. Yildiz (✉)
Faculty of Engineering and Natural Sciences (FENS), Sabanci University, Orhanli, Tuzla, 34956 Istanbul, Turkey
E-mail: meyildiz@sabanciuniv.edu

J. J. Feng
Department of Mathematics, University of British Columbia, Vancouver, BC V6T 1Z2, Canada

J. J. Feng
Department of Chemical and Biological Engineering, University of British Columbia, Vancouver, BC V6T 1Z3, Canada

fluids using linear stability analysis, pointing out the importance of conductivity in the liquid. Shankar and Sharma [15] conducted a similar study for leaky dielectric fluids using lubrication theory. Craster and Matar [13] investigated the instabilities in thin films in the nonlinear regime and reported the effects of fluid properties on the formation of instabilities. In these studies the electric field direction is perpendicular to the interface. Tilley et al. [16] investigated small-amplitude capillary waves on a non-conducting (perfect dielectric) liquid sheet subject to a parallel electric field and showed that the electrical force delays rupture in the sheet. Further extension to arbitrary amplitudes was carried out by Papageorgiou and Vanden-Broeck [17]. The effects of parallel and perpendicular electric fields on the evolution of the interface in (pressure driven) channel flows were studied by Uguz and Aubry [18]. Their results show that both parallel and perpendicular electric fields may be used to stabilize or destabilize the interface.

The studies mentioned above disregarded gravity because of the dominating role of electrical and capillary forces. One configuration where gravity plays an important role in driving the flow is Rayleigh-Taylor Instability (RTI). First observed by Lord Rayleigh [19] and Taylor [20], the instability happens when a heavier fluid sits atop a lighter one. The effects of an external electric field on the RTI have been well studied [11,21–25]. Mohamed and Shehawey [21] investigated the effects of a perpendicular electric field for perfect dielectric fluids using the method of multiple-scale perturbations. Their results show that the electric field may stabilize or destabilize the interface depending on the electric permittivity and density ratios. Elbade [23] studied the effects of parallel electric field and identified a stabilizing regime for RTI of inviscid perfect dielectric fluids. Barannyk et al. [25] further investigated this case for the limit of thin upper layer and reported a periodic motion at the interface for large enough electric fields. Joshi et al. [24] derived the dispersion relation for perturbation at the interface, emphasizing the viscous and leaky dielectric nature of the fluids. Most of the studies on electrohydrodynamic RTI are limited to the linear regime, and little has been done on the nonlinear development on longer time scales. To our knowledge, the only exception is Cimpeanu et al. [11], who performed Direct Numerical Simulation (DNS) of RTI in perfect dielectric medium subject to parallel electric field and found the results in the linear regime to be in agreement with their linear stability analysis. They further investigated the nonlinear regime using DNS and proposed a method for modulating the interface using timed electric field application.

Another limitation of the prior studies is their use of the perfect dielectric model. In reality, conductivity plays an important role in the evolution of interfacial forces in most fluids of interest [24,26,27]. The evolution of RTI in viscous leaky dielectric fluids in the presence of an external electric field involves complex interaction of surface and body forces. In this regard, a close observation of the interfacial forces and vorticity generation may provide valuable information regarding the later stages of the RTI evolution. To this end, we simulate RTI perturbed by a small-amplitude cosine wave subject to a perpendicular electric field. Unlike a parallel field, a perpendicular electric field does not result in suppression of the instability, allowing us to study the effects at later stages of the evolution.

Our results show that within the range of the parameters covered, the surface charges play an important role in shaping the interface. The electrical forces are concentrated on either of the bubble or the spike tips, depending on the parameters, and compete with the surface tension forces. The dominant mechanism in vorticity generation is found to be the surface tension force. However, the electric forces show comparable role at later stages of the simulation for higher field strengths.

## 2 Mathematical formulation

### 2.1 Governing equations of the fields

The equations governing electric and flow fields are evolved simultaneously for two incompressible, immiscible, isothermal, Newtonian and leaky dielectric fluids. Governing equations describing the evolution of the flow field may be written as

$$\nabla \cdot \mathbf{u} = 0, \tag{1}$$

$$\rho \frac{D\mathbf{u}}{Dt} = -\nabla p + \nabla \cdot \boldsymbol{\tau} + \mathbf{f}_{(b)} + \mathbf{f}_{(s)} + \mathbf{f}_{(e)}, \tag{2}$$

where $\mathbf{u}$ is the velocity vector, $p$ is pressure, $\rho$ is density, $t$ is time and $D/Dt = \partial/\partial t + \mathbf{u} \cdot \nabla$ represents the material time derivative. Viscous stress tensor $\boldsymbol{\tau}$ is defined as

$$\boldsymbol{\tau} = \mu \left[ \nabla \mathbf{u} + (\nabla \mathbf{u})^{\dagger} \right], \tag{3}$$

where superscript $\square^\dagger$ denotes the transpose operation. Here, $\mathbf{f}_{(b)}$, $\mathbf{f}_{(s)}$ and $\mathbf{f}_{(e)}$ are gravity, surface tension and electrical forces and will be defined in Sect. 2.2.

Assuming small dynamic currents and neglecting the magnetic induction effects, we have an irrotational electric field governed by Gauss' Law and charge conservation equation [28]. Further assumption of short electric relaxation time in comparison with viscous relaxation time simplifies these equations into [4,29]

$$\nabla \cdot (\sigma \nabla \phi) = 0, \tag{4}$$
$$q^v = \nabla \cdot (\varepsilon \nabla \phi), \tag{5}$$

where $\sigma$ and $\varepsilon$ denote electrical conductivity and permittivity of the fluid, respectively, $q^v$ is the volumetric representation of the surface charge density and the electric field is expressed in terms of an electric potential, $\phi$, as $\mathbf{E} = -\nabla \phi$.

To distinguish between different phases, a color function $\hat{c}$ is defined such that it is zero for the heavier fluid and unity for the other. Thermodynamic variables, transport coefficients, interface curvature and unit normals are computed using corresponding color function values [30].

## 2.2 Interfacial and body forces

In this section, we define the body and interfacial forces introduced in Eq. (2). Being a body force, gravity is treated directly as

$$\mathbf{f}_{(b)} = \rho \mathbf{g}, \tag{6}$$

where $\mathbf{g}$ is the gravitational acceleration vector. For computational efficiency and simplicity, the local surface tension force is expressed as an equivalent volumetric force [31], $\mathbf{f}_{(s)}$. Replacing the sharp interface between two fluids with a transitional region of finite thickness, surface tension force may be formulated as

$$\mathbf{f}_{(s)} = \gamma \kappa \hat{\mathbf{n}} \delta, \tag{7}$$

where $\delta$ is the Dirac delta function computed as the gradient of color function, and $\gamma$ is the constant surface tension coefficient. The interface curvature $\kappa$ is found through $-\nabla \cdot \hat{\mathbf{n}}$, where $\hat{\mathbf{n}}$ is the unit surface normal vector.

The stress induced by the external electric field on the flow is given by Maxwell stress tensor [4,32,33]. The equivalent volume force exerted on the flow is found by taking the divergence of the Maxwell stress tensor as

$$\mathbf{f}_{(e)} = -\frac{1}{2}\mathbf{E} \cdot \mathbf{E}\nabla \varepsilon + q^v \mathbf{E}. \tag{8}$$

The first term on the right-hand side, called the polarization force (dielectric force) $\mathbf{f}_{(ep)}$, will always act in a direction normal to the interface. The second term (called Coulomb force) $\mathbf{f}_{(eq)}$, is a result of interactions between electric field and electric charges and will be oriented in the direction of the electric field. The resultant electric force has a complex behavior which will be discussed further in Sect. 3.2.

## 2.3 Contribution of the interfacial forces to the vortex sheet strength

Following Dopazo et al. [34] and Wu [35], the vortex sheet strength on an infinitesimal path of length $\delta_\omega$ perpendicular to the interface may be written as

$$\Gamma = \int_{-\delta_\omega/2}^{0} \omega_l \mathrm{d}n + \int_{0}^{\delta_\omega/2} \omega_h \mathrm{d}n. \tag{9}$$

Here subscripts $\square_h$ and $\square_l$ denote heavy and light fluid sides, respectively. The contribution of pressure to $\mathrm{D}\Gamma/\mathrm{D}t$ may be written as

$$\hat{\mathbf{n}} \times \left\| \frac{1}{\rho}\nabla p \right\| = \hat{\mathbf{n}} \times \nabla \left\| \frac{p}{\rho} \right\|, \tag{10}$$

where $\|f\| = f_h - f_l$. Rearranging $\|p/\rho\|$ into

$$\left\| \frac{p}{\rho} \right\| = \frac{\|p\|}{\rho_h} - \left( \frac{1}{\rho_l} - \frac{1}{\rho_h} \right) p_l \tag{11}$$

and considering the stress balance on the interface [29], one may rewrite the left-hand side of equation (10) as

$$\hat{\mathbf{n}} \times \left\| \frac{1}{\rho} \boldsymbol{\nabla} p \right\| = -\hat{\mathbf{n}} \times \frac{\boldsymbol{\nabla} \left( \hat{\mathbf{n}} \cdot \mathbf{f}_{(e)} + \hat{\mathbf{n}} \cdot \mathbf{f}_{(s)} \right)}{\bar{\rho} \left( 1 + \mathcal{A} \right)} - \hat{\mathbf{n}} \times \frac{2\mathcal{A}}{\bar{\rho} \left( 1 - \mathcal{A}^2 \right)} \boldsymbol{\nabla} p_l, \tag{12}$$

where both fluids have identical viscosities while $\mathcal{A}$ and $\bar{\rho}$ denote Atwood number and average density, respectively. The first term on the right-hand side of the above equation will be computed to study the effects of the interfacial forces on vortex sheet strength. Although the above definition assumes an infinitesimally thin interface, we employ the forces used to evolve a diffuse representation of the interface in our simulations. As such, the forces are interpolated at the nominal location of the interface (0.5 level contour of color function) before calculating Eq. (12).

2.4 Dimensionless form of the equations

To better identify the effective parameters and ratios affecting the evolution of RTI, Eqs. (1), (2), (4) and (5) are made dimensionless assuming the following characteristic scales

$$\mathbf{x}' = \frac{\mathbf{x}}{W}, \qquad t' = \frac{t}{\sqrt{W/g_\infty}}, \qquad \mathbf{u}' = \frac{\mathbf{u}}{\sqrt{g_\infty W}}, \qquad \kappa' = \kappa W, \tag{13}$$
$$p' = \frac{p - \rho \mathbf{g} \cdot \mathbf{x}}{\bar{\rho} g_\infty W}, \qquad \rho' = \frac{\rho}{\bar{\rho}}, \qquad \mathbf{g}' = \frac{\mathbf{g}}{g_\infty},$$
$$\mathbf{E}' = \frac{\mathbf{E}}{E_\infty}, \qquad \phi' = \frac{\phi}{E_\infty W}, \qquad q' = \frac{q^v}{\bar{\varepsilon} E_\infty / W},$$

where $\bar{\square}$ denotes arithmetic average between heavier and lighter fluid values. $W$ is the width of the computational domain, while $E_\infty$ and $g_\infty$ denote undisturbed electric field strength and gravitational acceleration, respectively. In addition, ratios of heavy to light fluid values are defined as

$$\mathcal{A} = \frac{\rho_h - \rho_l}{2\bar{\rho}}, \qquad \mathcal{V} = \frac{\mu_h - \mu_l}{2\bar{\mu}}, \qquad \mathcal{P} = \frac{\varepsilon_h - \varepsilon_l}{2\bar{\varepsilon}}, \qquad \mathcal{C} = \frac{\sigma_h - \sigma_l}{2\bar{\sigma}}. \tag{14}$$

Here, $\mathcal{A}$ is Atwood number, $\mathcal{V}$ is viscosity ratio, $\mathcal{P}$ is permittivity ratio and $\mathcal{C}$ is conductivity ratio. Implementing these scales, the aforementioned equations may be rewritten as

$$\boldsymbol{\nabla}' \cdot \mathbf{u}' = 0, \tag{15}$$
$$\rho' \frac{\mathrm{D} u'}{\mathrm{D} t'} = -\boldsymbol{\nabla}' p' + \frac{1}{\mathrm{Re}} \boldsymbol{\nabla}' \cdot \boldsymbol{\tau}' + \frac{1}{\mathrm{Bo}} \mathbf{f}'_{(s)} + \frac{1}{\mathrm{Eg}} \mathbf{f}'_{(e)}, \tag{16}$$
$$\boldsymbol{\nabla}' \cdot \left( \sigma' \boldsymbol{\nabla} \phi' \right) = 0, \tag{17}$$
$$q' = \boldsymbol{\nabla}' \cdot \left( \varepsilon' \boldsymbol{\nabla}' \phi' \right), \tag{18}$$

where

$$\mathrm{Re} = \frac{\bar{\rho} \sqrt{g_\infty W^3}}{\bar{\mu}}, \quad \mathrm{Bo} = \frac{\bar{\rho} g_\infty W^2}{\gamma}, \quad \mathrm{Eg} = \frac{\bar{\rho} g_\infty W}{\bar{\varepsilon} E_\infty^2}, \tag{19}$$

are Reynolds, Bond and electro-gravitational numbers [36], respectively. Taking Re, Bo, $\mathcal{A}$ and $\mathcal{V}$ constant, the remaining effective parameters are Eg, $\mathcal{P}$ and $\mathcal{C}$, allowing this study to assess the effects of electrical properties and electric field intensity on the evolution of the instability. The motivation behind choosing $\mathcal{P}$ and $\mathcal{C}$ in their current form is to determine the force directions by observing the sign of these parameters. Further implications of this choice is illustrated in Sect. 3.3 and the "Appendix".

From this point forward, we drop the primes when referring to dimensionless values. To maintain the relative magnitude of the interfacial forces when comparing them, $\mathbf{f}_{(s)}$ and $\mathbf{f}_{(e)}$ are normalized with the same scale as the left-hand side of Eq. (16), $\bar{\rho} g_\infty$.

2.5 Numerical method

The governing equations are discretized using Incompressible Smoothed Particle Hydrodynamics (ISPH) method. Details of the method and extensive validation are provided by Shadloo et al. [29,37]. A summary of the numerical procedure is provided here. Indices referring to particles are given as upright subscripts.

To ensure a smooth transition between the properties of each phase when used for their interpolation, the color function $\hat{c}$ is smoothed out across the phase boundaries [29] as

$$c_i = \frac{1}{\psi_i} \sum_{j=1}^{J_n} \hat{c}_j W_{ij}. \tag{20}$$

Here, $\psi_i = \sum_{j=1}^{J_n} W_{ij}$, is the number density of SPH particle i, calculated as the sum of the interpolation kernel of neighboring particles i and j over all neighbors of particle i, $J_n$. The interpolation kernel $W(r_{ij}, h)$, concisely noted as $W_{ij}$, is a function of the magnitude of distance vector, $\mathbf{r}_{ij} = \mathbf{r}_i - \mathbf{r}_j$, between particle of interest i and its neighboring particles j and $h$, the smoothing length. The smoothed color function is also utilized to evaluate $\delta \simeq |\nabla c|, \kappa = -\nabla \cdot \hat{\mathbf{n}}$ and $\hat{\mathbf{n}} = \nabla c / |\nabla c|$ in Eq. (7) [30,37].

A predictor–corrector scheme is employed to advance the governing equations of flow in time using a first-order Euler approach with variable timestep according to Courant-Friedrichs-Lewy condition, $\Delta t = \zeta h / u_{max}$, where $u_{max}$ is the largest particle velocity magnitude and $\zeta$ is taken to be equal to 0.25 [37,38]. In predictor step all the variables are advanced to their intermediate form using following relations,

$$\mathbf{r}_i^* = \mathbf{r}_i^{(n)} + \mathbf{u}_i^{(n)} \Delta t + \delta \mathbf{r}_i^{(n)}, \tag{21}$$

$$\mathbf{u}_i^* = \mathbf{u}_i^{(n)} + \frac{1}{\rho_i^{(n)}} \left( \frac{1}{\mathrm{Re}} \nabla \cdot \boldsymbol{\tau}_i + \frac{1}{\mathrm{Bo}} \mathbf{f}_{(s)i} + \frac{1}{\mathrm{Eg}} \mathbf{f}_{(e)i} \right)^{(n)} \Delta t, \tag{22}$$

$$\psi_i^* = \psi_i^{(n)} - \Delta t \psi_i^{(n)} \left( \nabla \cdot \mathbf{u}_i^* \right), \tag{23}$$

where starred variables represent intermediate values, $\delta \mathbf{r}_i$ is the artificial particle displacement vector [37] and superscript $(n)$ denotes values at the $n$th time step.

Using intermediate values, pressure at the next time step is found by solving the Poisson equation which is then followed by corrections in position and velocity of the particles, completing the temporal transition.

$$\nabla \cdot \left( \frac{1}{\rho_i^*} \nabla p_i^{(n+1)} \right) = \frac{\nabla \cdot \mathbf{u}_i^*}{\Delta t}, \tag{24}$$

$$\mathbf{u}_i^{(n+1)} = \mathbf{u}_i^* - \frac{1}{\rho_i^*} \nabla p_i^{(n+1)} \Delta t, \tag{25}$$

$$\mathbf{r}_i^{(n+1)} = \mathbf{r}_i^{(n)} + \frac{1}{2} \left( \mathbf{u}_i^{(n)} + \mathbf{u}_i^{(n+1)} \right) \Delta t + \delta \mathbf{r}_i^{(n)}. \tag{26}$$

Boundary conditions are enforced through multiple boundary tangent method described in [39] while first derivative and Laplace operator of vector and scalar functions are approximated through following expressions

$$\frac{\partial f_i^m}{\partial x_i^k} a_i^{kl} = \sum_{j=1}^{J_n} \frac{1}{\psi_j} \left( f_j^m - f_i^m \right) \frac{\partial W_{ij}}{\partial x_i^l}, \tag{27}$$

$$\frac{\partial}{\partial x_i^k} \left( \varphi_i \frac{\partial f_i^m}{\partial x_i^k} \right) a_i^{ml} = 8 \sum_{j=1}^{J_n} \frac{2\varphi_i \varphi_j}{\varphi_i + \varphi_j} \frac{1}{\psi_j} \left( f_i^m - f_j^m \right) \frac{r_{ij}^m}{r_{ij}^2} \frac{\partial W_{ij}}{\partial x_i^l}, \tag{28}$$

$$\frac{\partial}{\partial x_i^k} \left( \varphi_i \frac{\partial f_i}{\partial x_i^k} \right) \left( 2 + a_i^{kk} \right) = 8 \sum_{j=1}^{J_n} \frac{2\varphi_i \varphi_j}{\varphi_i + \varphi_j} \frac{1}{\psi_j} \left( f_i - f_j \right) \frac{r_{ij}^k}{r_{ij}^2} \frac{\partial W_{ij}}{\partial x_i^k}. \tag{29}$$

Here, $a_i^{kl} = \sum_{j=1}^{J_n} \frac{r_{ij}^k}{\psi_j} \frac{\partial W_{ij}}{\partial x_i^l}$ is a corrective tensor that eliminates particle inconsistencies [38], while $\varphi$ may denote density-inversed, viscosity, permittivity or conductivity, where appropriate.

The current method has been used successfully to simulate Rayleigh-Taylor instability [37] and motion of a neutrally buoyant droplet suspended in an external electric field [29].

## 3 Results

In this study Re, Bo, $\mathcal{A}$ and $\mathcal{V}$ are assumed to be constants and equal to 225, 150, 1/3 and 0, while $\mathcal{P}$, $\mathcal{C}$ and Eg are varied to study the effects of electrical forces. The computational domain consists of a rectangle of size $1 \times 4$ discretized by $80 \times 320$ particles arranged on a Cartesian grid. This corresponds to a uniform particle spacing of 1/80 for the base resolution. Top and bottom walls obey the no-slip condition and have a constant potential difference. Side walls allow slip but prohibit penetration. The electric field direction is fixed pointing downward and parallel to the side walls. To define heavier and lighter fluid regions, we assign an initial interfacial perturbation according to

$$\hat{c}(x, y) = \begin{cases} 0, & y > 2 + 0.025 \cos(2\pi x), \\ \\ 1, & y < 2 + 0.025 \cos(2\pi x). \end{cases} \tag{30}$$

Two sets of parameters, PN (Positive permittivity ratio $\mathcal{P} = 0.3$, Negative conductivity ratio $\mathcal{C} = -0.3$, Eg $= 90$) and NP (Negative permittivity ratio $\mathcal{P} = -0.3$, Positive conductivity ratio $\mathcal{C} = 0.3$, Eg $= 90$), are referred to as baseline cases. When studying the effects of each parameter, the other parameters are kept constant at the baseline values. First we establish the convergence of the numerical results with respect to spatial resolution. Then the baseline cases are compared to RTI with no electric field and the general behavior of the interfacial forces are presented. The effects of the electrical properties of the fluids are investigated by simulating RTI at different $\mathcal{P}$ and $\mathcal{C}$. Finally, by varying Eg, we study the effects of electric field intensity on the evolution of instability.

### 3.1 Spatial resolution

As the particles are initially arranged in an equally spaced Cartesian grid, Eq. (30) results in an interface with a resolution-dependent step-like pattern. While the computational method is extensively tested for RTI without an external electric field [37], addition of electric forces necessitates further confirmation of proper resolution. To test the effects of the resolution on the results, we simulate case NP with particle spacings of $\delta_p = 1/40$, 1/60, 1/80, 1/100 and 1/120 and compare the results.

Figure 1 plots the simulation results where we call the lowest point of the heavier fluid the "spike tip" ($\square_s$) and the highest point of the lighter fluid the "bubble tip" ($\square_b$). Interface profiles are taken at moments when the spike reaches the following positions: $y_s = 1.7, 1.4, 1.1, 0.8$ and 0.5. Due to its initial step-like nature, the interface retains a slightly sinuous profile during the simulation. This results in a wavy pattern in surface tension force as it depends on the second derivative of the color function (*cf.* Figs. 3, 4). However, as it is seen in Fig. 1a and b, position and velocity profiles are quite similar for 1/80 and finer particle spacings. The interface profiles in the vicinity of the spike and bubble (Fig. 1c) have similar structures as well. Based on these observations and considering that this study focuses mostly on the behavior of the spike and bubble regions, the base resolution is found adequate.

### 3.2 Effects of an external electric field

To identify the effects of the electric field on Rayleigh-Taylor instability, the evolution of baseline cases are compared to that of a case with No Electric field, NE. Figure 2 provides spike and bubble tip positions and velocities along with snapshots of interface profiles at $y_s = 1.7, 1.4, 1.1, 0.8$ and 0.5. For case NP, the electric field affects the position of the spike tip much more than the bubble tip. The spike moves faster while the bubble is slightly slower. The opposite is true for case PN where the bubble is the faster feature. When compared at similar spike tip position, the longer side tails of case PN may also be attributed to its faster bubble ascent.

To better demonstrate the force composition (and analyze its effects) along the interface, Figs. 3 and 4 provide the force components perpendicular to the interface versus normalized interface length at spike tip position $y_s = 1.4$. A superscript $\square^n$ is used to denote the normal component when necessary. A positive value indicates a force pointing from heavier fluid to the lighter one. The only tangential component (not shown) applied to the interface is due to $\mathbf{f}_{(eq)}$ which is an order of magnitude smaller than its normal component and two orders of magnitude smaller than the surface tension force.
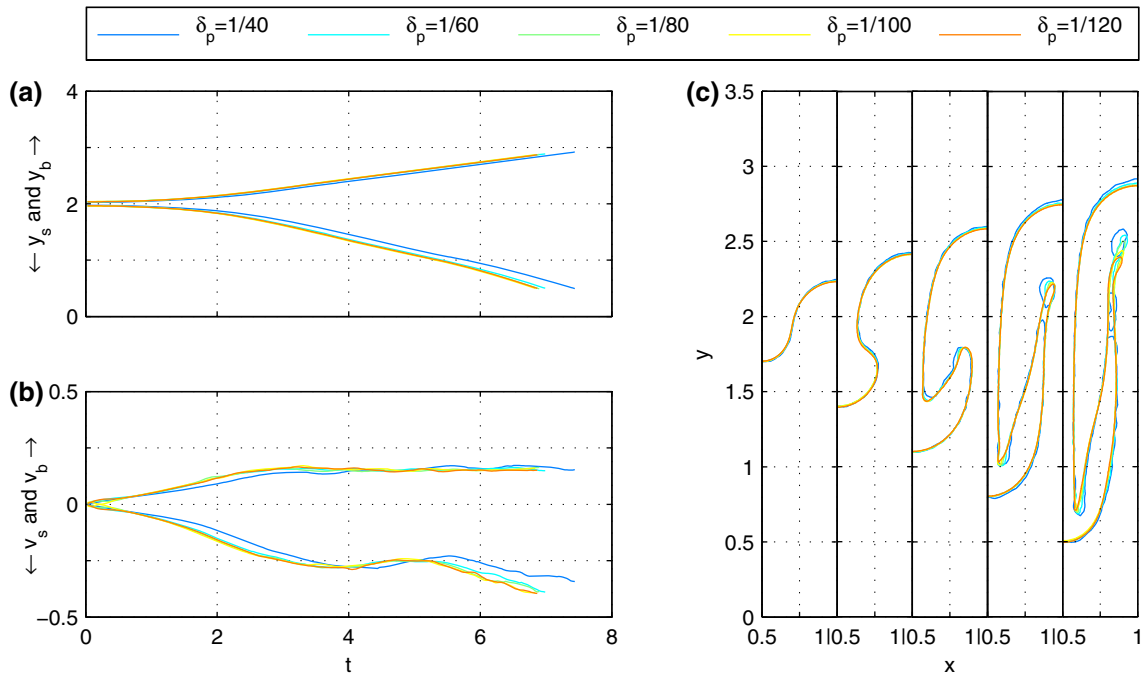
**Fig. 1** Spike and bubble tip positions (**a**) and velocities (**b**) versus time for different particle spacings of $\delta_p = 1/40, 1/60, 1/80, 1/100$ and $1/120$; **c** interface profiles at $y_s = 1.7, 1.4, 1.1, 0.8$ and $0.5$
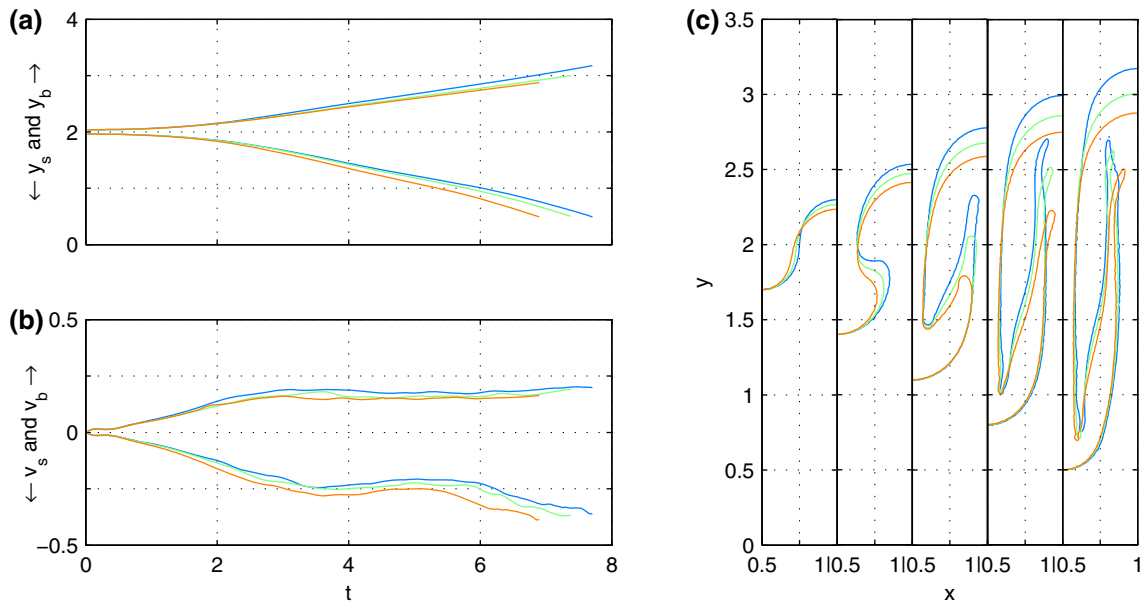


**Fig. 2** Spike and bubble tip positions (**a**) and velocities (**b**) for cases NP (*red*), PN (*blue*) and NE (*green*); **c** interface profiles at $y_s = 1.7, 1.4, 1.1, 0.8$ and $0.5$

Figures 3b and 4b show the normal electric force $\mathbf{f}_{(e)}^n$ and its components, $\mathbf{f}_{(ep)}$ and $\mathbf{f}_{(eq)}^n$, as defined in Eq. (8). The polarization force $\mathbf{f}_{(ep)}$ always points in the opposite direction of the permittivity gradient, i.e. toward the heavier fluid for case NP and in reverse direction for case PN. The Coulomb force $\mathbf{f}_{(eq)}$ is only parallel to the electric field and its direction is dependent on $q$. At this stage of the simulation, the extrema of $\mathbf{f}_{(eq)}^n$ occur at the spike tip, bubble tip and the relatively flat region between the two inflection points along the interface. $\mathbf{f}_{(ep)}$ has a smaller and relatively uniform magnitude along the interface when compared to $\mathbf{f}_{(eq)}^n$.
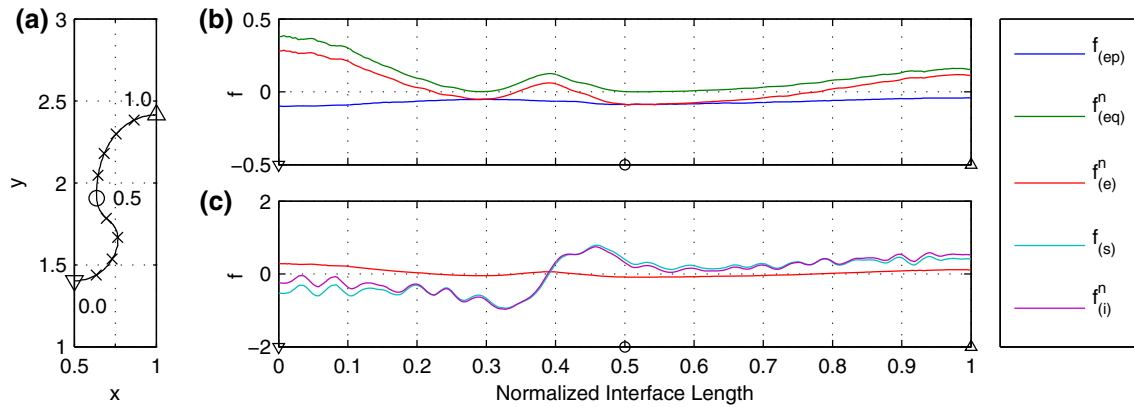
**Fig. 3** Profiles of normal force magnitudes along the interface for case NP; **a** interface profile; **b** electrical force and its components; **c** electrical force, surface tension and the resultant interfacial force; the cross marks on the interface are placed at 0.1 intervals of normalized interface length. Symbols on the interface and horizontal axes correspond to spike tip (*down triangle*), middle point of interface (*circle*) and bubble tip (*triangle*)
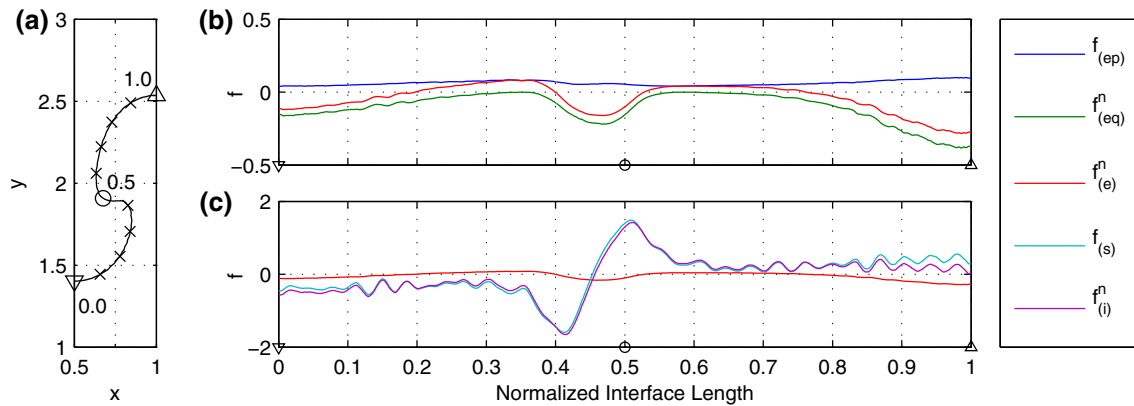


**Fig. 4** Profiles of normal force magnitudes along the interface for case PN; **a** interface profile; **b** electrical force and its components; **c** electrical force, surface tension and the resultant interfacial force; the cross marks on the interface are placed at 0.1 intervals of normalized interface length. Symbols on the interface and horizontal axes correspond to spike tip (*down triangle*), middle point of interface (*circle*) and bubble tip (*triangle*)

Figures 3c and 4c plot the electric force $\mathbf{f}^n_{(e)}$, surface tension $\mathbf{f}_{(s)}$ and their summation $\mathbf{f}^n_{(i)}$. Compared to the surface tension, which is larger at sharper corners of the interface, the electric force is almost negligible except at bubble tip (case PN) or spike tip (case NP). The role of the resultant electric force in these cases may be described as that of countering the hindrance of surface tension force which tends to minimize the surface energy by reducing the curvature. In case NP, the total force on the spike region is reduced due to the presence of the external electric field, while the impeding force on the bubble is slightly increased. Having the inverse force configuration, case PN experiences the opposite situation where bubble ascent is less prohibited and spike descent is slightly more hindered. This results in faster bubble ascent for case PN and faster spike descent for case NP, as observed in Fig. 2.

### 3.3 Effects of electrical permittivity and conductivity ratios

To study the effects of the permittivity ratio, the conductivity ratio is kept constant at $\mathcal{C} = \pm 0.3$, while $\mathcal{P}$ is varied from $-0.9$ to $+0.9$ in steps of 0.2. As for the effects of the conductivity ratio, $\mathcal{P} = \pm 0.3$ while $\mathcal{C}$ is varied from $-0.5$ to $+0.5$ in steps of 0.2.

Figure 5 shows spike and bubble positions and velocities with respect to time for constant $\mathcal{C}$. The arrows show the direction of increasing permittivity ratio $\mathcal{P}$. The effect of increase in $\mathcal{P}$ is identical for both $\mathcal{C} = \pm 0.3$, resulting in an increase in bubble ascent velocity while hindering the spike descent. Comparing the two cases,
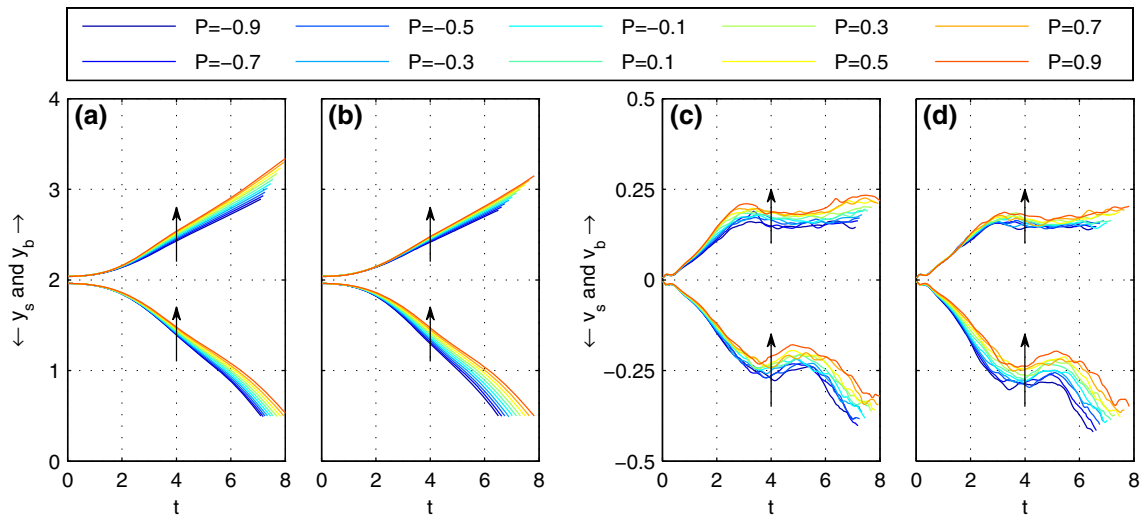
**Fig. 5** Spike and bubble tip position (**a**, **b**) and velocity (**c**, **d**) for $\mathcal{C} = -0.3$ (**a**, **c**) and $\mathcal{C} = +0.3$ (**b**, **d**); the *arrow* shows the direction of increasing $\mathcal{P}$
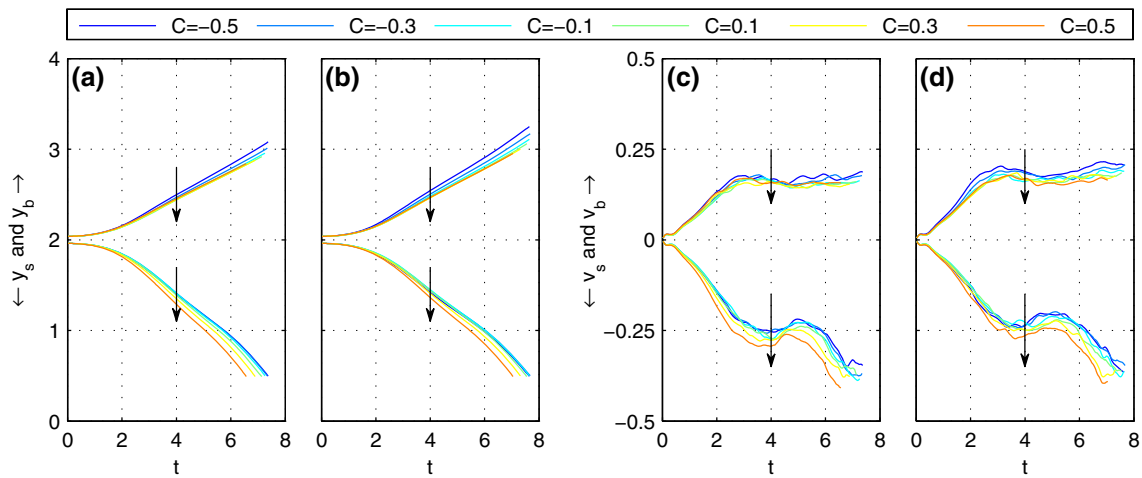


**Fig. 6** Spike and bubble tip position (**a**, **b**) and velocity (**c**, **d**) for $\mathcal{P} = -0.3$ (**a**, **c**) and $\mathcal{P} = +0.3$ (**b**, **d**); the *arrow* shows the direction of increasing $\mathcal{C}$

it is notable that the effects are more pronounced in the spike for $\mathcal{C} = +0.3$, while the bubble is more affected in $\mathcal{C} = -0.3$. Assuming that the bubble or the spike tip of different cases passing through the same height experience the same electric field, it is seen that $\mathbf{f}_{(e)}$ and its components $\mathbf{f}_{(ep)}$ and $\mathbf{f}_{(eq)}$ have a linear relationship with $\mathcal{P}$ (*cf.* "Appendix"). Increasing $\mathcal{P}$ at constant $\mathcal{C}$ increases $\mathbf{f}_{(e)}$ which in turn reduces the spike descent velocity and increases the bubble ascent velocity. For $\mathcal{C} < 0$, the electric field is stronger at larger $y$ thus having greater effect on the bubble, while $\mathcal{C} > 0$ has a similar effect on the spike (*cf.* Eq. (32) in "Appendix").

Figure 6 provides spike and bubble tip positions and velocities with respect to time for different $\mathcal{C}$ at constant $\mathcal{P}$. Increasing $\mathcal{C}$ reduces the ascent velocity of the bubble while increasing the descent velocity of the spike. For the range of parameters studied here, the bubble tip position tends to converge to a similar profile for $\mathcal{C} > 0$, whereas such convergence for the spike happens for $\mathcal{C} < 0$. A similar observation is valid for the tip velocities as well. The reason behind this behavior lies in the relation between electric field intensity and $\mathcal{C}$ (*cf.* Eq. (32) in "Appendix"). At $\mathcal{C} = 0$ the electric field intensity is uniform and equal to $E_{\infty}$. Further increase in $\mathcal{C}$ results in a reduction in electric field intensity at the bubble region. The difference in electric field intensity between consecutive levels of $\mathcal{C}$ is also reduced for larger $\mathcal{C}$. As a result, the electric force magnitude tends to converge to a minimum value at larger $\mathcal{C}$, as seen in Fig. 7 right for $\mathcal{P} = +0.3$. The reverse is true for the spike region where the electric force profiles converge for $\mathcal{C} < 0$ (Fig. 7 left). Figure 7 also shows surface tension
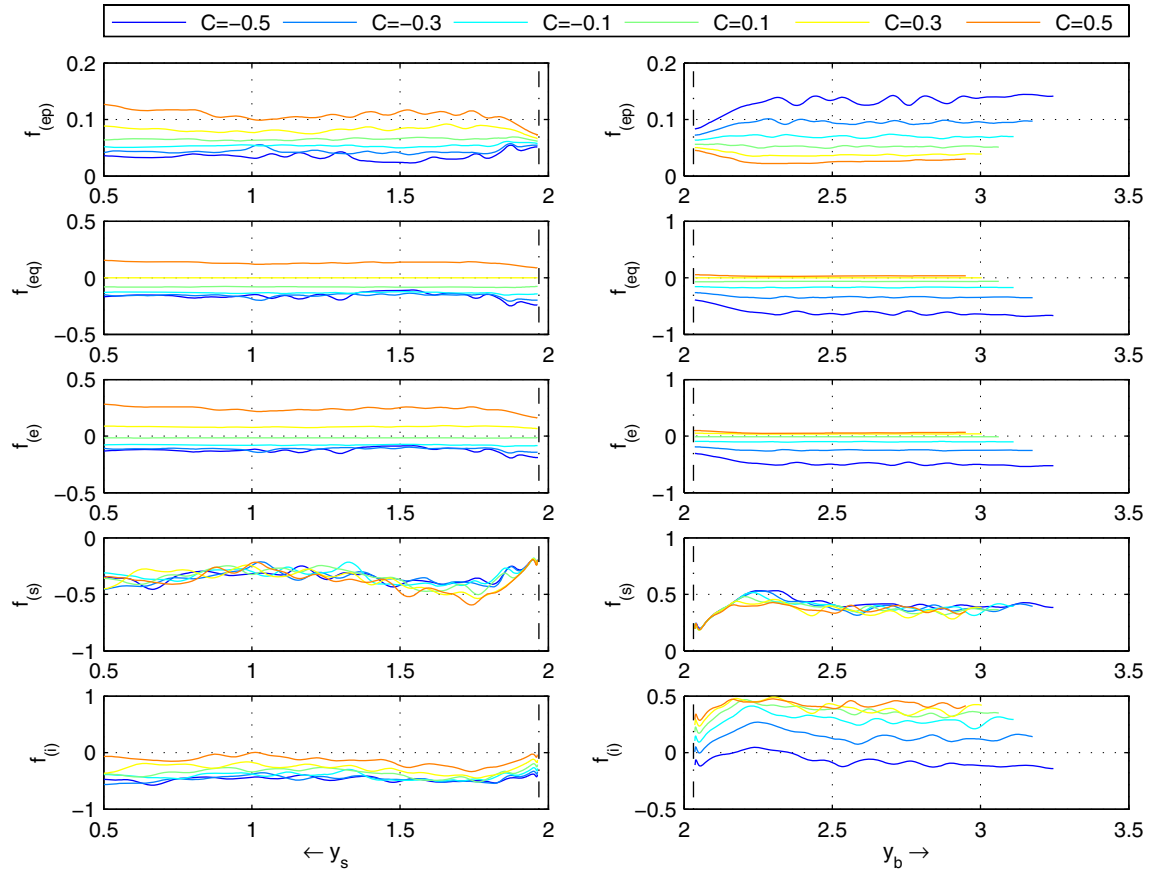
**Fig. 7** Magnitude of spike tip forces (*left*) and bubble tip forces (*right*) with respect to tip position for $\mathcal{P} = +0.3$. The *dash-dot line* shows the starting position of the spike and bubble tip. $\mathbf{f}_{(e)}$ is the electric force (*cf.* Eq. (8)), while $\mathbf{f}_{(ep)}$ and $\mathbf{f}_{(eq)}$ denote polarization and Coulomb components of the electric force, respectively. $\mathbf{f}_{(s)}$ is the surface tension force (*cf.* Eq. (7)) and $\mathbf{f}_{(i)}$ is the resultant interfacial forces

and resultant interfacial force for bubble and spike tips with respect to the related feature's position. Surface tension is mostly insensitive to changes in electrical properties. As expected, surface tension is the dominant interfacial force where electrical force has the smallest magnitude, i.e. for $\mathcal{C} < 0$ on the spike and for $\mathcal{C} > 0$ on the bubble. As a result, a converging profile is observed for each feature in its respective interval of $\mathcal{C}$. Similar observations are valid when $\mathcal{P} = -0.3$.

## 3.4 Effects of electric field intensity

### 3.4.1 Positions, velocities and interface profiles

To investigate the effects of the electric field intensity, the electro-gravitational number is started from 5.625 and multiplied by two for consecutive cases until Eg $= 360$ where a lower Eg denotes larger electric field intensity. The permittivity and conductivity ratio are kept at baseline values of NP and PN.

Figure 8 provides spike and bubble tip positions and velocities for both NP and PN baselines. Larger electric field intensities augment the effects observed in Sect. 3.2, i.e. an increase in the spike velocity and a decrease in the bubble velocity for NP. For PN, the reverse is true. The effects are more pronounced in the spike tip for NP and in the bubble tip for PN. After an initial movement at Eg $= 5.625$, the bubble and spike tips are almost stationary for cases NP and PN, respectively. Combined with the fast motion of the opposite feature, this results in significant deviations from the interface profiles for RTI at $\mathcal{A} = 1/3$ in the absence of the electric field which will be discussed further in the following paragraphs. The potential flow region (constant velocity
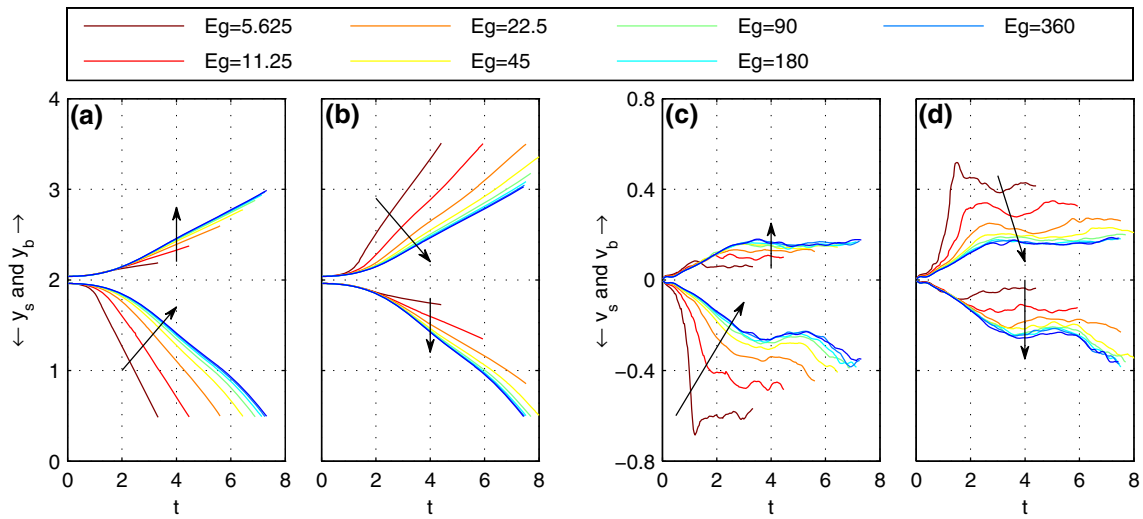
**Fig. 8** Spike and bubble tip position (**a**, **b**) and velocity (**c**, **d**) for NP ($\mathcal{P} = -0.3 - \mathcal{C} = +0.3$) (**a**, **c**) and PN ($\mathcal{P} = +0.3 - \mathcal{C} = -0.3$) (**b**, **d**); the *arrows* show the direction of increasing Eg (decreasing field intensity)
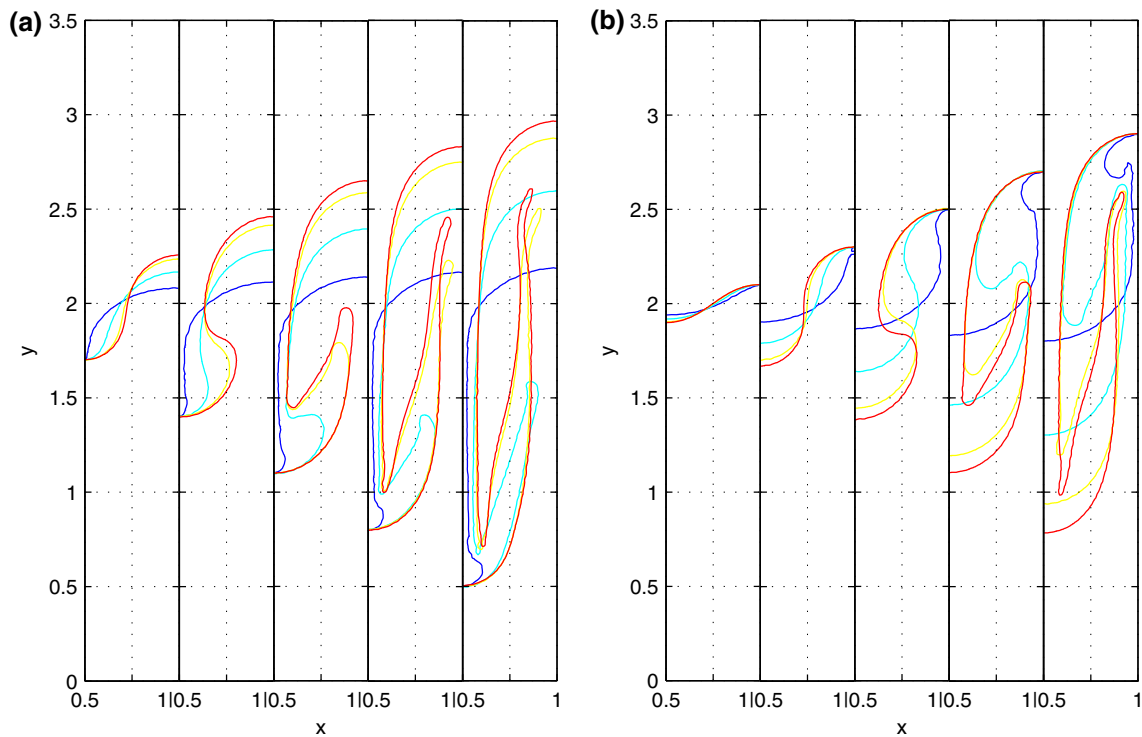


**Fig. 9** Interface profiles for Eg = 5.625 (*blue*), 22.5 (*cyan*), 90 (*yellow*) and 360 (*red*); **a** NP ($\mathcal{P} = -0.3 - \mathcal{C} = +0.3$) at spike height $y_s = 1.7, 1.4, 1.1, 0.8$ and $0.5$; **b** PN ($\mathcal{P} = +0.3 - \mathcal{C} = -0.3$) at bubble height $y_b = 2.1, 2.3, 2.5, 2.7$ and $2.9$

movement) of evolution is reached earlier at smaller Eg, while reacceleration of spike does not appear during the simulation times considered here.

Figure 9 plots interface profiles at Eg = 5.625, 22.5, 90 and 360. The interface profiles are shown at identical spike tip positions for NP. Fast spike motion and nearly stagnant bubble at Eg = 5.625 result in a lack of heavy fluid at the spike region. This in turn leads to a very small spike tip and thin stem with completely suppressed side tails. This behavior resembles that of very high $\mathcal{A}$ RTI. Increasing Eg results in thicker stem and well-developed side tails. As for PN, the interface profiles are plotted at identical bubble tip heights. At Eg = 5.625, the spike tip moves much slower than the bubble tip. This leads to a thick spike with a small
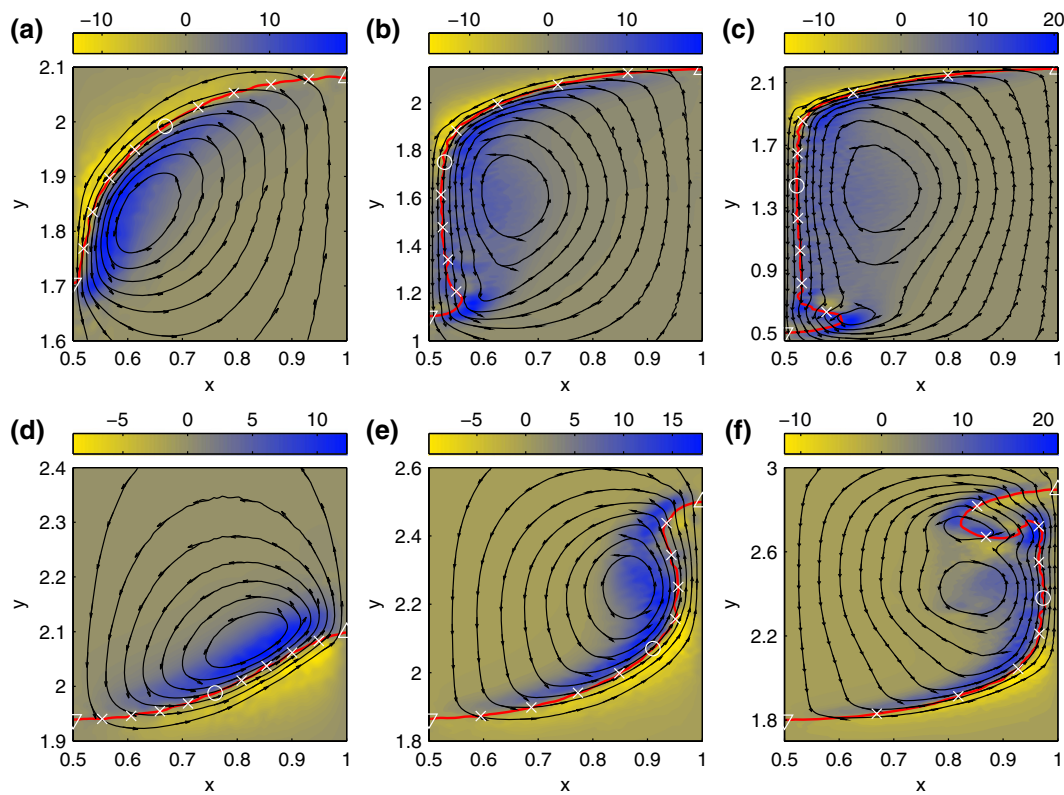
**Fig. 10** Contours of vorticity (*fills*) and streamlines (*lines*); the cross marks on the interface are placed at 0.1 intervals of normalized interface length. Symbols on the interface (Fig. 11 on the horizontal axes) correspond to spike tip (*down triangle*), middle point of interface (*circle*) and bubble tip (*triangle*). **a–c** NP with Eg = 5.625 at $y_s$ = 1.7, 1.1 and 0.5 (*blue* contours in Fig. 9a); **g–i** PN with Eg = 5.625 at $y_b$ = 2.1, 2.5 and 2.9 (*blue* contours in Fig. 9b)

structure rising at its side. This structure resembles bubbles rising in quiescent fluid at high Bo numbers (small surface tension). At Eg = 22.5, the spike and the bubble cover similar distances with respect to time, which is a feature of very low $\mathcal{A}$ RTI. By further increasing Eg, the profiles approach those in the absence of the electric field.

### 3.4.2 Vortical structures

To investigate the effects of the electric field intensity on the vortical structures, Fig. 10 shows vorticity contours and streamlines near the interface drawn in red at Eg = 5.625. The figure shows case NP at $y_s$ = 1.7, 1.1 and 0.5 and case PN at $y_b$ = 2.1, 2.5 and 2.9. These six panels correspond to those of Fig. 11 which depicts $\hat{\mathbf{n}} \times \nabla \left( \hat{\mathbf{n}} \cdot \mathbf{f}_{(e)} \right)$, $\hat{\mathbf{n}} \times \nabla \left( \hat{\mathbf{n}} \cdot \mathbf{f}_{(s)} \right)$ and their summation as a measure of the first term on the right-hand side of Eq. (12) along the interface. The interface is marked at 0.1 intervals of the normalized interface length on the contour lines of Fig. 10 and horizontal axes of Fig. 11, where symbols $\triangledown$, $\circ$ and $\triangle$ correspond to the spike tip, middle point of the interface and the bubble tip, respectively.

In Fig. 10, the single vortex generated at early stages of the simulation is highly skewed toward the heavier fluid for case NP and toward the lighter fluid for case PN. This structure, which rotates counter-clockwise, encompasses large regions of one fluid while leaving the other fluid almost stagnant, except near the interface (Fig. 10a, d). Vorticity generation sites are clearly observable near the tip of the preferred structure (spike for NP and bubble for PN) in Fig. 10b and e. Occasionally, counter-rotating vortices may emerge near the main vortex in the lighter fluid for case NP and in heavier fluid for case PN (not shown here). A co-rotating vortical structure emerges at the later stages shown in Fig. 10c and f. Such co-rotating vortices are not observed in our NE simulation. The co-rotating vortices of case PN merge as the bubble rises to $y_b$ = 3.8, while the co-rotating vortices in case NP persist during the simulation time (until $y_s$ = 0.2).

Figure 11 provides a measure of the role of the electric forces in generation of the observed vortical structures. The very early stages involving generation of small co-rotating vortices are similar to that of the
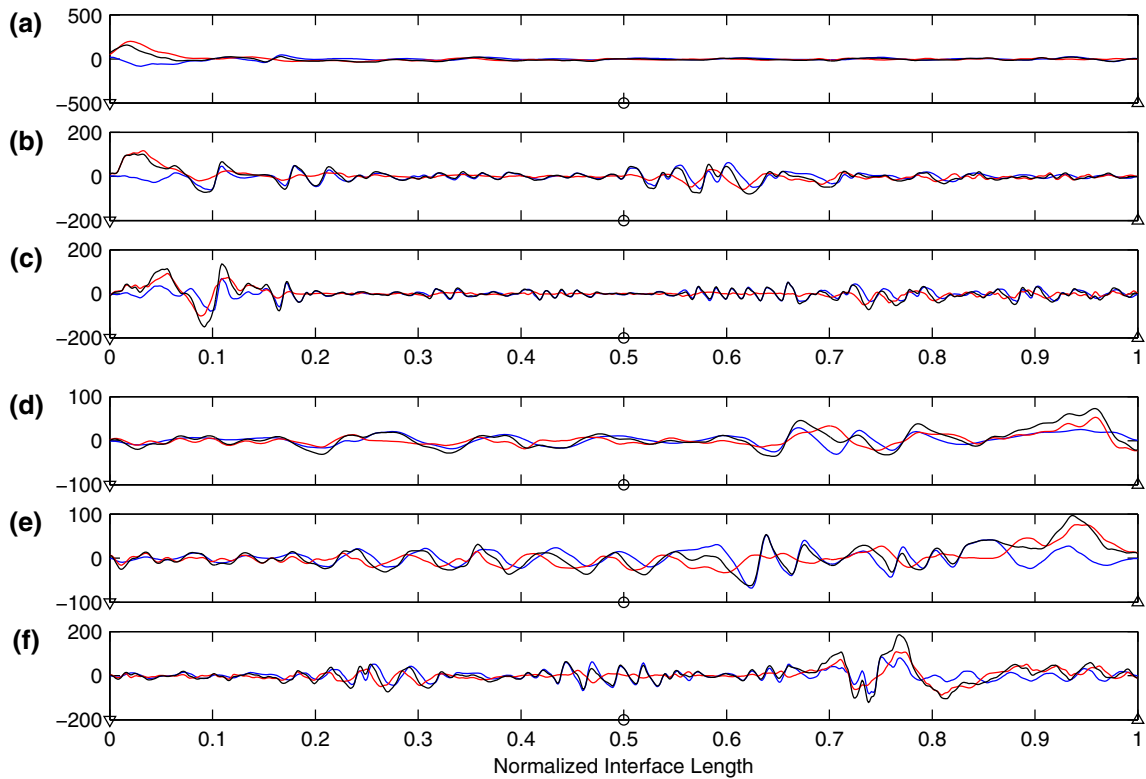
**Fig. 11** Electric force (*red*), surface tension (*blue*) and resultant contribution of interfacial forces (*black*) on vortex sheet strength in right-hand side of Eq. (12); symbols on the horizontal axes correspond to spike tip (*down triangle*), middle point of interface (*circle*) and bubble tip (*triangle*). These symbols correspond to those in Fig. 10 on the interface. **a–c** NP with Eg = 5.625 at $y_s$ = 1.7, 1.1 and 0.5; **d–f** PN with Eg = 5.625 at $y_b$ = 2.1, 2.5 and 2.9

case NE (*cf.* Sect. 3.1). However, the rest of the evolution is different when large electric field values are used. As is seen in Fig. 11a and d, the dominant vorticity generation mechanism is through electric forces near the tip of the preferred structure (spike for NP and bubble for PN). As the features start to extend (Fig. 11b, e), additional sites are introduced where surface tension is the dominant generation mechanism. The sites dominated by the electric force also start to move away from the tips (Fig. 11c, f) which results in the generation of the smaller co-rotating vortex observed in Fig. 10c and f. At later stages of the simulation, both surface tension and electric forces play an equal role in vorticity generation.

## 4 Conclusion

Rayleigh-Taylor instability appears when a heavier fluid is above a less dense one in a gravitational field. Manipulation of this instability using electric fields has been the subject of many studies. Most of these studies, however, are based on linearized or simplified models. In this study, incompressible immiscible RTI of leaky dielectric fluids is simulated until its late stages using Smoothed Particle Hydrodynamics method at Re = 225, Bo = 150, $\mathcal{A}$ = 1/3 and $\mathcal{V}$ = 0. The electric field is taken to be perpendicular to the initial interface so as to maintain the unstable evolution. Interfacial forces and vortex generation are studied to explain how the interfacial evolution is affected by the permittivity ratio, the conductivity ratio and the electric field intensity.

The results show that increasing the top-to-bottom permittivity ratio augments the rise of the bubble while hindering the descent of the spike. On the other hand, increasing the conductivity ratio results in a decrease in the bubble velocity while augmenting the spike movement. At large conductivity ratios, the bubble is more affected when the permittivity ratio is positive, whereas the spike is more affected when permittivity ratio is negative. Increasing the electric field intensity has different effects depending on the combination of the permittivity and conductivity ratios. Applying larger field intensities results in narrower structures. At higher

field intensities, electric forces dominate vorticity generation at early stages of the simulation. However, the role of surface tension and electric forces become comparable at later stages of the evolution.

To summarize, it is shown that manipulating the electric field intensity in conjunction with electrical properties of the fluids allow for control of the interfacial morphology by suppressing certain features while augmenting others.

## Appendix

To demonstrate the underlying relation between $\mathcal{P}, \mathcal{C}$ and $\mathbf{f}_{(e)}$, a simplification for flat regions is derived here. As bubble and spike tips have relatively flat surfaces, this will provide further insight about the behavior of these structures with respect to $\mathcal{P}$ and $\mathcal{C}$. Using dimensional form of the variables and starting with the definition of a divergence free electric field (Eq. (4)), it is possible to approximate the divergence of the electric field across the interface as

$$\nabla \cdot \mathbf{E} \approx -\bar{\mathbf{E}} \cdot \frac{\nabla \sigma}{\bar{\sigma}}. \tag{31}$$

It is notable that the strength of electric field due to finite potential $\Delta \phi$ on a flat interface depends on its position with respect to the electrodes $y$ and $\mathcal{C}$ as

$$\bar{\mathbf{E}} \approx \frac{\Delta \phi}{(H - y)(1 - \mathcal{C}) + y(1 + \mathcal{C})} \hat{\mathbf{n}}, \tag{32}$$

where $H$ is the distance between electrodes. Without a loss in generality, it is assumed that $\bar{\sigma} = \bar{\varepsilon}$ and test cases are set according to this assumption. Upon setting $\nabla f = -\delta \hat{\mathbf{n}} \Delta f$, where $\Delta f = f_h - f_l$ represents permittivity or conductivity difference between heavy and light fluids, one may rewrite Eq. (5) as

$$q^v \approx -2\bar{\varepsilon}\delta\bar{\mathbf{E}} \cdot \hat{\mathbf{n}} (\mathcal{P} - \mathcal{C}). \tag{33}$$

As noted before, positive normal vector points from heavier fluid to the lighter one in this study. This means that surface normal and electric field vector point in the same direction on the flat portions of the interface. Consequently, approximations of $\mathbf{f}_{(eq)}$ and $\mathbf{f}_{(ep)}$ follow as

$$\mathbf{f}_{(eq)} \approx -2\bar{\varepsilon}\delta (\mathcal{P} - \mathcal{C}) \bar{\mathbf{E}}^2 \hat{\mathbf{n}}, \quad \mathbf{f}_{(ep)} \approx \bar{\varepsilon}\delta\mathcal{P}\bar{\mathbf{E}}^2 \hat{\mathbf{n}}, \tag{34}$$

while $\mathbf{f}_{(e)}$ may be approximated as

$$\mathbf{f}_{(e)} \approx -\bar{\varepsilon}\delta (\mathcal{P} - 2\mathcal{C}) \bar{\mathbf{E}}^2 \hat{\mathbf{n}}. \tag{35}$$

Equations (32), (34) and (35) provide a coarse approximation to the electric field and the electric force applied to the bubble and the spike tip regions, facilitating a general observation of the trends.

## References

1. Taylor, G.: Studies in electrohydrodynamics. I. The circulation produced in a drop by an electric field. Proc. R. Soc. Lon. Ser. A **291**(1425), 159–166 (1966). doi:10.1098/rspa.1966.0086
2. Melcher, J.R., Schwarz, W.J.: Interfacial relaxation overstability in a tangential electric field. Phys. Fluids **11**(12), 2604–2616 (1968). doi:10.1063/1.1691866
3. Melcher, J.R., Taylor, G.I.: Electrohydrodynamics: a review of role of interfacial shear stresses. Annu. Rev. Fluid Mech. **1**, 111–146 (1969). doi:10.1146/annurev.fl.01.010169.000551
4. Saville, D.A.: Electrohydrodynamics: the Taylor-Melcher leaky dielectric model. Annu. Rev. Fluid Mech. **29**, 27–64 (1997). doi:10.1146/annurev.fluid.29.1.27
5. Chen, X.P., Jia, L.B., Yin, X.Z., Cheng, J.S., Lu, J.: Spraying modes in coaxial jet electrospray with outer driving liquid. Phys. Fluids **17**(3), 032101 (2005). doi:10.1063/1.1850691
6. Higuera, F.J.: Stationary coaxial electrified jet of a dielectric liquid surrounded by a conductive liquid. Phys. Fluids **19**(1), 012102 (2007). doi:10.1063/1.2431188
7. Li, G., Luo, X., Si, T., Xu, R.X.: Temporal instability of coflowing liquid-gas jets under an electric field. Phys. Fluids **26**(5), 054101 (2014). doi:10.1063/1.4875109

8. Higuera, F.J.: Electrodispersion of a liquid of finite electrical conductivity in an immiscible dielectric liquid. Phys. Fluids **22**(11), 112107 (2010). doi:10.1063/1.3493636
9. Oddy, M.H., Santiago, J.G., Mikkelsen, J.C.: Electrokinetic instability micromixing. Anal. Chem. **73**(24), 5822–5832 (2001). doi:10.1021/ac0155411
10. El Moctar, A.O., Aubry, N., Batton, J.: Electro-hydrodynamic micro-fluidic mixer. Lab Chip **3**(4), 273–280 (2003). doi:10.1039/b306868b
11. Cimpeanu, R., Papageorgiou, D.T., Petropoulos, P.G.: On the control and suppression of the Rayleigh-Taylor instability using electric fields. Phys. Fluids **26**(2), 022105 (2014). doi:10.1063/1.4865674
12. Warner, M.R.E., Craster, R.V., Matar, O.K.: Pattern formation in thin liquid films with charged surfactants. J. Colloid Interface Sci. **268**(2), 448–463 (2003). doi:10.1016/j.jcis.2003.08.013
13. Craster, R.V., Matar, O.K.: Electrically induced pattern formation in thin leaky dielectric films. Phys. Fluids **17**(3), 032104 (2005). doi:10.1063/1.1852459
14. Pease, L.F., Russel, W.B.: Electrostatically induced submicron patterning of thin perfect and leaky dielectric films: a generalized linear stability analysis. J. Chem. Phys. **118**(8), 3790–3803 (2003). doi:10.1063/1.1529686
15. Shankar, V., Sharma, A.: Instability of the interface between thin fluid films subjected to electric fields. J. Colloid Interface Sci. **274**(1), 294–308 (2004). doi:10.1016/j.jcis.2003.12.024
16. Tilley, B.S., Petropoulos, P.G., Papageorgiou, D.T.: Dynamics and rupture of planar electrified liquid sheets. Phys. Fluids **13**(12), 3547–3563 (2001). doi:10.1063/1.1416193
17. Papageorgiou, D.T., Vanden-Broeck, J.M.: Large-amplitude capillary waves in electrified fluid sheets. J. Fluid Mech. **508**, 71–88 (2004). doi:10.1017/S0022112004008997
18. Uguz, A.K., Aubry, N.: Quantifying the linear stability of a flowing electrified two-fluid layer in a channel for fast electric times for normal and parallel electric fields. Phys. Fluids **20**(9), 092103 (2008). doi:10.1063/1.2976137
19. Rayleigh, L.: Investigation of the character of the equilibrium of an incompressible heavy fluid of variable density. Proc. Lond. Math. Soc **s1–14**(1), 170–177 (1882). doi:10.1112/plms/s1-14.1.170
20. Taylor, G.: The instability of liquid surfaces when accelerated in a direction perpendicular to their planes I. Proc. R. Soc. Lond. Ser. A **201**(1065), 192–196 (1950). doi:10.1098/rspa.1950.0052
21. Mohamed, A.E.M.A., Shehawey, E.S.F.E.: Nonlinear electrohydrodynamic Rayleigh-Taylor instability. Part 1. A perpendicular field in the absence of surface charges. J. Fluid Mech. **129**, 473–494 (1983). doi:10.1017/S0022112083000877
22. Mohamed, A.E.M.A., El Shehawey, E.S.F.: Nonlinear electrohydrodynamic Rayleigh-Taylor instability. II. A perpendicular field producing surface charge. Phys. Fluid **26**(7), 1724–1730 (1983). doi:10.1063/1.864371
23. Eldabe, N.T.: Effect of a tangential electric-field on Rayleigh-Taylor instability. J. Phys. Soc. Jpn. **58**(1), 115–120 (1989). doi:10.1143/JPSJ.58.115
24. Joshi, A., Radhakrishna, M.C., Rudraiah, N.: Rayleigh-Taylor instability in dielectric fluids. Phys. Fluids **22**(6), 064102 (2010). doi:10.1063/1.3435342
25. Barannyk, L.L., Papageorgiou, D.T., Petropoulos, P.G.: Suppression of Rayleigh-Taylor instability using electric fields. Math. Comput. Simul **82**(6,SI), 1008–1016 (2012). doi:10.1016/j.matcom.2010.11.015
26. Pease, L.F., Russel, W.B.: Linear stability analysis of thin leaky dielectric films subjected to electric fields. J. Non-Newton. Fluid Mech **102**(2, SI), 233–250 (2002). doi:10.1016/S0377-0257(01)00180-X
27. Thaokar, R.M., Kumaran, V.: Electrohydrodynamic instability of the interface between two fluids confined in a channel. Phys. Fluids **17**(8), 084104 (2005). doi:10.1063/.1.979522
28. Hua, J., Lim, L.K., Wang, C.H.: Numerical simulation of deformation/motion of a drop suspended in viscous liquids under influence of steady electric fields. Phys. Fluids **20**(11), 113302 (2008). doi:10.1063/1.3021065
29. Shadloo, M.S., Rahmat, A., Yildiz, M.: A smoothed particle hydrodynamics study on the electrohydrodynamic deformation of a droplet suspended in a neutrally buoyant Newtonian fluid. Comput. Mech. **52**, 693–707 (2013). doi:10.1007/s00466-013-0841-z
30. Tofighi, N., Yildiz, M.: Numerical simulation of single droplet dynamics in three-phase flows using ISPH. Comput. Math. Appl. **66**(4), 525–536 (2013). doi:10.1016/j.camwa.2013.05.012
31. Brackbill, J.U., Kothe, D.B., Zemach, C.: A continuum method for modeling surface-tension. J. Comput. Phys. **100**(2), 335–354 (1992). doi:10.1016/0021-9991(92)90240-Y
32. Tomar, G., Gerlach, D., Biswas, G., Alleborn, N., Sharma, A., Durst, F., Welch, S.W.J., Delgado, A.: Two-phase electrohydrodynamic simulations using a volume-of-fluid approach. J. Comput. Phys. **227**(2), 1267–1285 (2007). doi:10.1016/j.jcp.2007.09.003
33. Melcher, J.R., Smith, C.V.: Electrohydrodynamic charge relaxation and interfacial perpendicular-field instability. Phys. Fluids **12**(4), 778–790 (1969). doi:10.1063/1.1692556
34. Dopazo, C., Lozano, A., Barreras, F.: Vorticity constraints on a fluid/fluid interface. Phys. Fluids **12**(8), 1928–1931 (2000). doi:10.1063/1.870441
35. Wu, J.Z.: A theory of three-dimensional interfacial vorticity dynamics. Phys. Fluids **7**(10), 2375–2395 (1995). doi:10.1063/1.868750
36. IEEE Trans. Dielectr. Electr. Insul. Recommended international standard for dimensionless parameters used in electrohydrodynamics. **10**(1), 3–6 (2003). doi:10.1109/TDEI.2003.1176545
37. Shadloo, M.S., Zainali, A., Yildiz, M.: Simulation of single mode Rayleigh-Taylor instability by SPH method. Comput. Mech. **51**(5), 699–715 (2013). doi:10.1007/s00466-012-0746-2
38. Zainali, A., Tofighi, N., Shadloo, M.S., Yildiz, M.: Numerical investigation of Newtonian and non-Newtonian multiphase flows using ISPH method. Comput. Methods Appl. Mech. Eng. **254**, 99–113 (2013). doi:10.1016/j.cma.2012.10.005
39. Yildiz, M., Rook, R.A., Suleman, A.: SPH with the multiple boundary tangent method. Int. J. Numer. Methods Eng. **77**(10), 1416–1438 (2009). doi:10.1002/nme.2458